A mesoporous nanoenzyme derived from metal–organic frameworks with endogenous oxygen generation to alleviate tumor hypoxia for significantly enhanced photodynamic therapy

Wang, Dongdong; Wu, Huihui; Lim, Wei Qi; Phua, Fiona Soo Zeng; Xu, Pengping; Chen, Qianwang; Guo, Zhen; Zhao, Yanli

2019

Wang, D., Wu, H., Lim, W. Q., Phua, F. S. Z., Xu, P., Chen, Q., ... Zhao, Y. (2019). A mesoporous nanoenzyme derived from metal–organic frameworks with endogenous oxygen generation to alleviate tumor hypoxia for significantly enhanced photodynamic therapy. Advanced Materials, 31(27), 1901893-. doi:10.1002/adma.201901893

Submitted to ADVANCED MATERIALS

DOI: 10.1002/adma.((please add manuscript number))

Article type: Communication

Mesoporous Nanoenzyme Derived from Metal-Organic Frameworks with Endogenous Oxygen Generation to Alleviate Tumor Hypoxia for Significantly Enhanced Photodynamic Therapy

Dongdong Wang, Huihui Wu, Wei Qi Lim, Soo Zeng Fiona Phua, Pengping Xu, Qianwang Chen, Zhen Guo,* Yanli Zhao**

Dr. D. Wang, W. Q. Lim, S. Z. F. Phua, Prof. Y. L. Zhao
Division of Chemistry and Biological Chemistry
School of Physical and Mathematical Sciences
Nanyang Technological University
21 Nanyang Link, Singapore 637371, Singapore
E-mail: zhaoyanli@ntu.edu.sg

H. Wu, Prof. Z. Guo
School of Life Sciences
University of Science and Technology of China
Hefei 230026, P. R. China
E-mail: zhenguo@ustc.edu.cn

P. Xu, Prof. Q. Chen
Hefei National Laboratory for Physical Sciences at Microscale
Department of Materials Science & Engineering
University of Science and Technology of China
Hefei 230026, P. R. China
E-mail: cqw@ustc.edu.cn

Keywords: endogenous oxygenation • H_2O_2-activation • hypoxia alleviation • metal-organic frameworks • photodynamic therapy

Abstract

Tumor hypoxia compromises the therapeutic efficiency of photodynamic therapy (PDT) as the local oxygen concentration plays an important role in the generation of cytotoxic singlet oxygen ($^1O_2$). Herein, we present a versatile mesoporous nanoenzyme (NE) derived from metal-organic frameworks (MOFs) for *in situ* generation of endogenous O_2 to enhance the PDT efficacy under the bioimaging guidance. The mesoporous NE was constructed by first coating manganese-based MOFs with mesoporous silica, followed by a facile annealing process under ambient atmosphere. After removing the mesoporous silica shell and post-modifying with polydopamine and polyethylene glycol for improving the biocompatibility, the obtained mesoporous NE was loaded by Ce6, a commonly used photosensitizer in PDT, with a high loading capacity. Upon the O_2 generation through the catalytic reaction between catalytic amount NE and endogenous H_2O_2, the hypoxic tumor microenvironment was relieved. Thus, Ce6-loaded NE served as an H_2O_2-activated oxygen supplier to increase the local O_2 concentration for significantly enhanced antitumor PDT efficacy *in vitro* and *in vivo*. In addition, the NE also showed T_2-weighted magnetic resonance imaging ability for its *in vivo* tracking. This work presents an interesting biomedical use of MOF-derived mesoporous NE as a multifunctional theranostic agent in the cancer therapy.

Photodynamic therapy (PDT), a well-known clinical modality that involves photosensitizer, molecular oxygen (O_2), and excitation light to generate cytotoxic reactive oxygen species such as singlet oxygen ($^1O_2$), has been proven to be a selective method for treating a wide spectrum of localized and superficial cancers or other diseases.[1-9] In addition to destroying cancer cells through direct photodamage, PDT can also induce vascular damage in the tumor, and activate the response of immune system.[10-13] Possessing spatial and temporal control over the localization of the light irradiation, the O_2-involved PDT can remarkably improve the selectivity and reduce the side effects when compared to other conventional modalities such as chemotherapy, surgery and radiotherapy.[14-16] On the other hand, tumor hypoxia compromises therapeutic effect of PDT, as O_2 is an indispensable element during the process. Uncontrollable growth of tumor cells as well as dysregulated formation of tumor blood vessels inevitably result in the cancer hypoxia.[17,18] In addition, microvascular collapse caused by PDT would further compromise the O_2 supply and aggravate the hypoxia condition, thus preventing effective PDT of cancer. Consequently, a vicious circle occurs, as PDT not only consumes localized O_2, but also cuts off the O_2 supply.[19-21]

To date, three main strategies have been employed to overcome the pre-existing hypoxia and improve the therapeutic effect of PDT. The most popular approach relies on the integration of PDT with other therapeutic modalities for a synergistic therapy.[17,22,23] However, such complex structures are often costly, which limit their scalable production and reproducibility. Another strategy is the utilization of intelligent nanomaterials that can act as O_2 carriers for direct transportation of molecular oxygen to tumor sites. For example, Hu and coworkers reported photosensitizer-loaded perfluorocarbon nanodroplets as an O_2 self-enriched PDT nanoplatform.[24] The last approach is to construct smart nanoplatforms for *in situ* generation of O_2 within solid tumors based on the characteristics of tumor microenvironment. Interestingly, tumors often over-express hydrogen peroxide (H_2O_2, usually at a generation rate of 5 nmol/10^5 cells h^{-1}), and H_2O_2 could be a source for O_2 production within tumors.[25-28] Thus, various kinds of nanoparticle-based catalysts/enzymes have been constructed to catalyze the decomposition of H_2O_2 to generate O_2 for ameliorating tumor hypoxia, including MnO_2,[29-31] CaO_2,[32,33] carbon nitride,[34,35] carbon dots,[36-38] biological catalase,[39-41] and others.[42-45] These reported nanoplatforms have shown outstanding catalytic activity for *in situ* endogenous O_2 generation, consequently leading to high therapeutic effect on account of the production of highly cytotoxic $^1O_2$ under NIR light irradiation.[36,46,47] However, some major challenges still exist. For instance, excess use of nanoplatforms and photosensitizers to ensure O_2 generation and therapeutic efficacy would cause side effects such as repeated administration and severe light sensitivity.[48,49] Meanwhile, unpredictable toxicity of some reported nanoparticles obviously limit their future clinical applications.[50-52] As the catalysts, continuous catalytic ability and long-time durability are preferred. For the well-known MnO_2-based nanomaterials, a major disadvantage is their rapid pH-responsive degradation to further compromise the PDT efficacy, as continuous O_2 generation is vital during the therapeutic process. Thus, there is an urgent need for the construction of biocompatible therapeutic systems that could catalyze the O_2 generation continuously and produce more cytotoxic $^1O_2$ for enhanced PDT.

In this work, we designed a multifunctional mesoporous nanoenzyme (NE) that could catalyze endogenous H_2O_2 decomposition for efficient O_2 generation to achieve imaging-guided augmented PDT. This system comprising mesoporous manganese cobalt oxide ($Mn_{1.8}Co_{1.2}O_4$ = MnCoO) derived from $Mn_3[Co(CN)_6]_2$ metal-organic frameworks (MOFs) was further modified with polydopamine (PDA) and polyethylene glycol (PEG) to give the MnCoO-PDA-PEG (MCOPP) NE (Scheme 1). Taking advantage of intrinsic properties of MOFs, the mesoporous structure was retained during the one-step annealing process. The

resultant MCOPP NE exhibited good physiological stability, negligible biological toxicity, and improved tumor accumulation. The efficient decomposition of endogenous H_2O_2 for rapid O_2 generation by the MCOPP NE without self-consumption or external activation indicates its durable catalytic ability as compared to the existing technology. Moreover, the MCOPP NE could also serve as a T_2-weighted magnetic resonance (MR) imaging contrast agent, allowing for its *in vivo* tracking. Chlorin e6 (Ce6) was chosen as the photosensitizer to be loaded into MCOPP on account of favorable coordination between deprotonated COO^- and catalytically active sites such as Mn^{2+}. After loading Ce6, the obtained MCOPP-Ce6 could successfully ameliorate tumor hypoxia for significantly enhanced PDT efficiency.

Figure 1a illustrates the stepwise synthesis and surface modification of MCOPP NE for the O_2 generation and enhanced $^1O_2$ production. Firstly, the $Mn_3[Co(CN)_6]_2$ MOFs were fabricated using a co-precipitation method.[53,54] Transmission electron microscopy (TEM) images reveal that the as-prepared MOF nanoparticles had a cubic morphology and were uniformly dispersed with an average diameter of 75 nm (Figure S1, Supporting Information). The MOF nanoparticles were then coated with a mesoporous silica shell *via* the Stöber method.[45] The average diameter of resulted MnCo@SiO_2 nanoparticles is 100 nm with uniform size distribution (Figure S2, Supporting Information). The MnCo@SiO_2 nanoparticles were treated by a facile one-step annealing strategy in air atmosphere under 500 °C for 4 hours. Through removing the mesoporous silica shell by NaOH aqueous solution, monodispersed MnCoO nanoparticles with an average size of ~80 nm were obtained (Figure S3, Supporting Information). It should be noted that mesoporous silica coated on MnCoO could avoid the particle aggregation during the annealing process. Powder X-ray diffraction (PXRD) pattern of the obtained MnCoO nanoparticles (Figure S4, Supporting Information) present typical spinel crystal phase of manganese cobalt oxide (JCPDS 18-0410). High-resolution TEM (HRTEM) images of the MnCoO nanoparticles clearly show that small manganese cobalt oxide particles are distributed throughout the mesoporous MnCoO nanoparticles (Figure S5, Supporting Information). Meanwhile, representative lattice fringe spacing of 0.249 and 0.299 nm agrees well with the crystal lattice of (211) and (112) planes for the manganese cobalt oxide phase. The elemental mapping of the MnCoO nanoparticles indicates that the Mn, Co and O elements are homogeneously distributed throughout the entire structure, validating the successful preparation from the MOF precursor (Figure S6, Supporting Information).

The MnCoO nanoparticles were further functionalized with amino groups (-NH_2) through coating PDA under mild alkaline condition, followed by PEGylation with PEG-SCM (SCM =

succinimide) to obtain the MCOPP NE. TEM image in Figure 1b shows that the MCOPP NE presents good monodispersity with an average size of ~85 nm. The hydrodynamic diameter of the MCOPP NE is about 100 nm due to the presence of PEG chains (Figure S7, Supporting Information) and shows no obvious change in diameter even after 24 days of storage at 25 °C (Figure S8, Supporting Information). The as-prepared MCOPP NE also exhibited excellent physiological stability when dispersed in saline, phosphate-buffered saline (PBS), and Dulbecco's modified eagle medium even for 10 months at 4 °C. The changes in zeta potential among MnCoO (-16.1 ± 1.2 mV), MnCoO-PDA (4.5 ± 1.8 mV) and MCOPP NE (-11.6 ± 1.7 mV) suggest the successful stepwise modification of the PDA shell and PEG chains (Figure S9, Supporting Information). The r_2 relaxivity of the MCOPP NE was calculated to be 56.4 mM^{-1} s^{-1} using a 3T clinical MR scanner, exhibiting an obvious concentration-dependent darkening effect (Figure 1c and inset). Nitrogen adsorption and desorption isotherms of the MCOPP NE present a typical H_3 hysteresis loop, indicating its mesoporous nature (Figure S10, Supporting Information). Brunauer-Emmett-Teller surface area and pore volume were calculated to be 456.6 m^2 g^{-1} and 0.475 cm^3 g^{-1}, respectively. The mesoporous property and large surface area make MCOPP NE a suitable nanosystem for loading photosensitizers. The loading capacity of Ce6 was calculated to be 13.8% according to the UV-vis measurements (Figure S11, Supporting Information). Such high loading capacity could be attributed to the coordination between deprotonated carboxylate groups in Ce6 and metal ion species in the mesoporous channels of the MCOPP NE under mild alkaline conditions.[55]

The O_2 generation capacity of the MCOPP NE at a high H_2O_2 concentration was shown in the Supporting Information (Movie 1), demonstrating that O_2 was rapidly generated upon the contact of the NE with H_2O_2. After homogenous mixing of the MCOPP NE with low concentration of H_2O_2 (1 mM) at room temperature, a significant amount of O_2 bubbles could also be observed (Figure 1d and inset). The O_2 concentration in the tested solution after adding the MCOPP NE was maintained at a consistently high level for 40 min. To quantitatively evaluate the catalytic ability, time-dependent H_2O_2 assays were performed upon the addition of the MCOPP NE (Figure 1e), showing that more than 50% of H_2O_2 was decomposed by the MCOPP NE within 12 min and completely depleted within 3 h (Figure 1f and S12, Supporting Information). Benefited from the porous nanostructure of the NE to offer more active reaction sites, the calculated catalytic reaction rate constant toward the H_2O_2 decomposition at room temperature is 0.0438 min^{-1}, which is higher than those of widely reported MnO_2 (0.0233 min^{-1}) and Mn-based carbon dots (0.0194 min^{-1}) (Figure S13, Supporting Information).[36,56] The experimental results clearly show that the catalytic ability

of MCOPP NE is much higher as compared with these reported materials. Moreover, its catalytic activity remained unchanged after several repeated additions of H_2O_2, indicating its excellent catalytic durability (Figure 1g).

Encouraged by the efficient O_2 generation of the MCOPP NE, we further investigated the $^1O_2$ production of MCOPP-Ce6 in the presence of H_2O_2 using electron spin resonance (ESR) technique with 2,2,6,6-tetramethylpiperidine (TEMP) as the $^1O_2$ trapping agent under 671 nm laser irradiation.[57] The MCOPP-Ce6 sample gave a typical 1:1:1 triplet signal (Figure 1h), which is the characteristic peak of $^1O_2$. The dramatic enhancement of $^1O_2$ generation in the presence of MCOPP-Ce6 could be accounted by the unique mesoporous character, which not only provides rich surface Mn atoms acting as the catalytic sites, but also reduces the diffusion distance between the *in situ* generated O_2 and photosensitizer. Considering the effective H_2O_2 catalytic ability, we wondered whether MCOPP-Ce6 could be an oxygen supplier for enhanced PDT efficacy at a mimetic H_2O_2 environment. Thus, the $^1O_2$ generation efficiency was determined using 1, 3-diphenylisobenzonfuran (DPBF) as an indicator, since its interaction with $^1O_2$ could induce irreversible absorbance bleaching of DPBF at 421 nm. As shown in Figure 1i, the $^1O_2$ production of MCOPP-Ce6 under hypoxic condition after light irradiation was lower than that under normoxic condition. Interestingly, the $^1O_2$ production by MCOPP-Ce6 under hypoxic condition was significantly enhanced when adding H_2O_2. Having the hypoxic atmosphere and mimetic H_2O_2 environment, the improved $^1O_2$ production could be explained by the O_2 supply generated by the MCOPP NE through the catalytic reaction.

Before confirming the catalytic ability of the MCOPP NE *in vitro*, standard 3-(4,5-dimethylthiazol-2-yl)-2,5-diphenyltetrazolium bromide (MTT) assay was performed to study its cytotoxicity. As shown in **Figure 2**a, the relative viability of 4T1 cells all remained over 90% even at a high concentration of 200 μg mL^{-1}. Concomitantly, the MCOPP NE also showed negligible cytotoxicity to HeLa cells, A549 tumor cells, and normal human embryonic kidney (HEK 293) cells after 24 h treatment under the same concentrations (Figures S14 and S15, Supporting Information). Therefore, subsequent *in vitro* experiments were carried out using the NE concentration at 200 μg mL^{-1} or less. Confocal laser scanning microscopy (CLSM) images and flow cytometry analysis showed higher MCOPP-Ce6 uptake by 4T1 cancer cells as compared with free Ce6 (Figure S16, Supporting Information), validating the need of this delivery vehicle to facilitate cellular accumulation of photosensitizers. We next investigated *in vitro* PDT efficiency of the MCOPP-Ce6 under normoxic and hypoxic conditions. Hypoxic atmosphere was realized by incubating 4T1 cells

in an incubator furnished with a hypoxic gas stream (volume ratio, N_2 : CO_2 : O_2 = 94 : 5 : 1) for 2 h before the treatments with various samples.[43] When performed under normoxic condition, free Ce6 and MCOPP-Ce6 groups exhibited comparable photo-toxicity toward 4T1 cells (Figure 2b). In contrast, the PDT efficiency of free Ce6 and MCOPP-Ce6 groups was compromised under hypoxic atmosphere due to insufficient O_2 supply (Figure 2c). Interestingly, when having 100 μM H_2O_2 to mimic the tumor environment followed by 671 nm laser irradiation, a killing efficacy of ~95.2% was achieved at 57 μg mL^{-1} of MCOPP-Ce6, realizing an enhanced PDT efficacy on account of sufficient O_2 supply generated *via* the catalytic reaction. To further validate the *in vitro* cell killing efficiency, Calcein AM (green, live cells) and propidium iodide (red, dead cells) co-staining assay was performed. When incubated with free Ce6, lower proportion of 4T1 cells was dead under hypoxic condition as compared with that under normoxic condition (Figure 2d). Remarkably, comparable red fluorescence was observed in the MCOPP-Ce6 group under hypoxic and normoxic conditions, confirming that the PDT efficiency was unaffected by the hypoxia. Furthermore, the intracellular ROS generation was tested by an ROS detection kit. After the cells were treated with MCOPP-Ce6, the ROS stress level in 4T1 cells significantly increased (Figure S17, Supporting Information). These results demonstrate that the MCOPP NE could ameliorate hypoxia in mimetic tumor condition and play a vital role in achieving high PDT efficiency.

We further investigated the intracellular O_2 generation for alleviating the hypoxia. An intracellular O_2 level indicator $[Ru(dpp)_3]Cl_2$ was used to detect the endogenous O_2 (Figure 2e).[58] Cells treated with the MCOPP NE group showed weaker fluorescence as compared with the control group under hypoxic condition, confirming significant intracellular O_2 generation from the MCOPP NE (50 μg mL^{-1}) *via* catalytic reaction. Upon increasing the MCOPP NE concentration from 50 to 100 μg mL^{-1}, much weaker red fluorescence signal was observed, indicating that the production of intracellular O_2 was concentration-dependent and hence the treatment efficiency could be easily modulated. It was established that hypoxic cells are characterized by intracellular accumulation of hypoxia-inducible factor HIF-1α protein.[59] Thus, we decided to understand the change in the level of HIF-1α after the *in vitro* treatment with the MCOPP NE. In a typical experiment, Alexa Fluor 488-conjugated primary antibody and rhodamine-conjugated phalloidin were used to co-stain HIF-1α and Tubulin, respectively. The expression of HIF-1α was also subjected to a Western blot analysis. As shown in Figure 2f, the control group showed highly expressed HIF-1α level under hypoxic condition. On the other hand, the HIF-1α protein was greatly down-regulated when increasing the concentration of incubated NE, while a similar amount of tubulin antibody was detected in the cell lysis.

Immunofluorescence imaging also indicated that the incubation of cells under normoxic condition showed no expression of hypoxia inducible factor HIF-1α, and a large amount of HIF-1α was accumulated under hypoxic condition. When 4T1 cells under hypoxic condition were treated with the MCOPP NE at different concentrations, significantly lower HIF-1α immunofluorescence was observed, suggesting that the efficient oxygen generation induced by the NE could attenuate the hypoxic condition (Figure 2g).

The PDT treatment efficiency of MCOPP-Ce6 was then determined *in vivo*. First, the circulation half-life was calculated to be 4.15 h by secondary exponential fitting (Figure S18, Supporting Information). The fairly long circulation time would benefit the accumulation of nanoparticles in the tumor site. Thereafter, *in vivo* MR imaging was performed to evaluate its capability of tumor imaging.[60] The MCOPP NE was administered into 4T1 tumor-bearing mice *via* intravenous injection. As shown in **Figure 3**a, T_2-weighted MR imaging signals at the tumor site gradually increased over time, exhibiting time-dependent tumor accumulation of the MCOPP NE through the enhanced permeability and retention (EPR) effect.[61-63] *In vivo* fluorescence was also performed. As shown in Figure 3b, MCOPP-Ce6 could accumulate within the tumor site. In addition, the MCOPP-Ce6 exhibited sustained Ce6 fluorescence at the tumor site for 24 h, indicating its good retention in the tumor tissue. Before performing *in vivo* therapy, the biocompatibility of the MCOPP NE was also studied. The hemolysis results indicated negligible hemolytic effect (2%) from the MCOPP NE even at a concentration as high as 1 mg mL^{-1} in PBS, demonstrating its favorable biocompatibility (Figure S19, Supporting Information). The biodistribution of the MCOPP NE in the major organs and tumor tissues were also investigated (Figure S20, Supporting Information). While showing some uptake in liver, kidney, and spleen mainly due to the macrophage engulfment in the reticuloendothelial systems,[64-66] the MCOPP NE could sufficiently accumulate in tumor sites with the efficiency of ~ 6.4% within 24 h.

Furthermore, immunofluorescence staining was performed to investigate the capability of the MCOPP NE for *in situ* amelioration of the tumor hypoxia by using pimonidazole hydrochloride as a hypoxyprobe.[67] Tumor hypoxic regions and its surrounding vessels were stained with anti-pimonidazole antibody (green fluorescence) and anti-mouse CD31 antibody (red fluorescence), respectively. As compared to the control group displaying bright green fluorescence, the tumor slices from the MCOPP NE treatment group exhibited significantly reduced hypoxic immunofluorescence (Figure 3c). The results suggest that the tumor hypoxia was alleviated on account of the catalytic conversion of H_2O_2 into O_2 by the MCOPP NE. In addition, semiquantitative statistical analysis of positive hypoxic regions and blood vessel

density calculated from ten confocal images revealed that the MCOPP NE could efficiently ameliorate the hypoxic condition in tumor microenvironment without detectable changes to the tumor vasculature (Figure 3d).

After studying the hypoxia amelioration ability of the MCOPP NE within tumor sites, we explored the PDT efficacy of Ce6 loaded MCOPP in 4T1 animal models. Tumor-bearing mice were randomly divided into six groups (n = 5). For mice undergoing PDT, the animals were subjected to 5 min of NIR light irradiation (671 nm, 100 mW cm^{-2}) at 24 h post intravenous injection. As expected, mice treated with saline (control, group I) and NIR light irradiation alone (group II) demonstrated the fastest tumor growth (Figure 3e). Similarly, free Ce6 (group III) and MCOPP-Ce6 (group IV) also witnessed no obvious influence on the tumor growth. The tumor growth in mice administrated with Ce6 plus NIR (group V) could partially be inhibited due to the PDT of Ce6 under NIR light irradiation (Figure 3f). Excitingly, remarkable tumor suppression was observed in mice treated with MCOPP-Ce6 and NIR light irradiation (group VI). On day 15, the mice were euthanized and the tumors from different treatment groups were harvested. The difference in the tumor mass (Figure 3g) was consistent with the tumor growth curve as shown in Figure 3e. In comparison to the PDT treatment by free Ce6, the PDT efficacy achieved by MCOPP-Ce6 was superior, suggesting a synergistic effect by increasing the local availability of O_2 and utilizing it to generate $^1O_2$ for self-sustained PDT. Next, the hematoxylin and eosin (H&E) analysis on tumor slices was performed to assess the enhanced therapeutic efficiency (Figure 3h). Prominent tumor tissue damage was noticed from the mice treated with MCOPP-Ce6 plus NIR light irradiation, further validating the PDT effect from the NE.

In addition, the animal body weight was also monitored during the PDT process to study whether the MCOPP-Ce6 has any systemic toxicity. As shown in **Figure 4**a, all treatment groups exhibited similar weight change as compared with their initial body weight. Finally, *in vivo* blood biochemistry and blood routine analysis were comprehensively conducted to investigate the long-term biotoxicity of MCOPP-Ce6. Blood from healthy mice was collected through the tail artery at different time points after intravenous injection of MCOPP-Ce6. All hepatic function and kidney function markers, including aspartate aminotransferase (AST), alkaline phosphatase (ALP), alanine transaminase (ALT), and blood urea nitrogen (BUN) were tested. The aminotransferase levels at day 7 and 15 were relatively similar to the control group, implying compatible hepatic and kidney property of MCOPP-Ce6 (Figure 4b,c). For the blood routine analysis, indexes such as white blood cell (WBC), red blood cells (RBC), hemoglobin (HGB), hematocrit (HCT), platelets (PLT), mean corpuscular volume (MCV),

mean platelet volume (MPV), mean corpuscular hemoglobin (MCH), and mean corpuscular hemoglobin concentration (MCHC) were determined (Figure 4d-l). All nine indexes fell within the normal ranges, revealing negligible *in vivo* blood toxicity of MCOPP-Ce6 at the treatment dose within 15 days.[68-70] The histological analysis on the main organ tissues from mice sacrificed 15 days post-treatment with MCOPP-Ce6 *via* tail vein injection was also performed (Figure 4m). No detectable signs of damaged tissues or inflammatory lesions were observed, indicating high histocompatibility of MCOPP-Ce6. All these results firmly demonstrate that MCOPP-Ce6 has a negligible systemic toxicity, potentiating its future application as an efficient therapeutic platform.

In summary, multifunctional mesoporous MCOPP derived from MOFs serving as a Fenton reaction NE has been successfully synthesized through the one-step annealing strategy and modifications with biocompatible PDA and PEG. Systematic *in vitro* and *in vivo* results have demonstrated that the hypoxia condition could be effectively alleviated through continuous O_2 generation by the catalytic reaction between endogenous H_2O_2 and MCOPP NE. The mesoporous MCOPP NE shows a high loading capacity to Ce6 photosensitizer, and the resulted MCOPP-Ce6 platform could remarkably enhance the therapeutic efficiency of PDT toward hypoxic tumor. Systemically administered MCOPP-Ce6 was selectively accumulated within tumor sites to continuously catalyze H_2O_2 into O_2, presenting excellent property for enabling simultaneous relief of tumor hypoxia and improved PDT efficacy. Thus, biocompatible MCOPP NE holds a great potential as an advanced theranostic system for achieving efficient cancer treatment.

Supporting Information

Supporting Information is available from the Wiley Online Library or from the author.

Acknowledgements

We thank the Core Facility Center for Life Sciences of University of Science and Technology of China for imaging support. The work was supported by the National Natural Science Foundation of China (21571168 and 31471268), and the Singapore National Research Foundation Investigatorship (NRF-NRFI2018-03).

Received: ((will be filled in by the editorial staff))

Revised: ((will be filled in by the editorial staff))

Published online: ((will be filled in by the editorial staff))

References

[1] D. W. Felsher, *Nat. Rev. Cancer* **2003**, *3*, 375.

[2] S. S. Lucky, K. C. Soo, Y. Zhang, *Chem. Rev.* **2015**, *115*, 1990.

[3] D. van Straten, V. Mashayekhi, H. de Bruijn, S. Oliveira, D. Robinson, *Cancers* **2017**, *9*, 19.

[4] C. Hopper, *Lancet Oncol.* **2000**, *1*, 212.

[5] Z. Zhen, W. Tang, Y. J. Chuang, T. Todd, W. Zhang, X. Lin, G. Niu, G. Liu, L. Wang, Z. Pan, X. Chen, J. Xie, *ACS Nano* **2014**, *8*, 6004.

[6] K. Lu, C. He, W. Lin, *J. Am. Chem. Soc.* **2014**, *136*, 16712.

[7] Y. Liu, Y. Liu, W. Bu, C. Cheng, C. Zuo, Q. Xiao, Y. Sun, D. Ni, C. Zhang, J. Liu, J. Shi, *Angew. Chem. Int. Ed.* **2015**, *54*, 8105.

[8] H. Gong, Y. Chao, J. Xiang, X. Han, G. Song, L. Feng, J. Liu, G. Yang, Q. Chen, Z. Liu, *Nano Lett.* **2016**, *16*, 2512.

[9] K. Han, S. B. Wang, Q. Lei, J. Y. Zhu, X. Z. Zhang, *ACS Nano* **2015**, *9*, 10268.

[10] Á. Juarranz, P. Jaén, F. Sanz-Rodríguez, J. Cuevas, S. González, *Clin. Transl. Oncol.* **2008**, *10*, 148.

[11] T. J. Dougherty, C. J. Gomer, B. W. Henderson, G. Jori, D. Kessel, M. Korbelik, J. Moan, Q. Peng, *J. Natl. Cancer Inst.* **1998**, *90*, 889.

[12] G. Yang, L. Xu, J. Xu, R. Zhang, G. Song, Y. Chao, L. Feng, F. Han, Z. Dong, B. Li, Z. Liu, *Nano Lett.* **2018**, *18*, 2475.

[13] B. Ding, S. Shao, C. Yu, B. Teng, M. Wang, Z. Cheng, K. L. Wong, P. Ma, J. Lin, *Adv. Mater.* **2018**, 1802479.

[14] I. Noh, D. Lee, H. Kim, C. U. Jeong, Y. Lee, J. O. Ahn, H. Hyun, J. H. Park, Y. C. Kim, *Adv. Sci.* **2018**, *5*, 1700481.

[15] B. Tian, C. Wang, S. Zhang, L. Feng, Z. Liu, *ACS Nano* **2011**, *5*, 7000.

[16] M. Abbas, Q. Zou, S. Li, X. Yan, *Adv. Mater.* **2017**, *29*, 1605021.

[17] C. Zhang, K. Zhao, W. Bu, D. Ni, Y. Liu, J. Feng, J. Shi, *Angew. Chem. Int. Ed.* **2015**, *54*, 1770.

[18] R. Xu, Y. Wang, X. Duan, K. Lu, D. Micheroni, A. Hu, W. Lin, *J. Am. Chem. Soc.* **2016**, *138*, 2158.

[19] M. G. Vander Heiden, L. C. Cantley, C. B. Thompson, *Science* **2009**, *324*, 1029.

[20] R. G. Bristow, R. P. Hill, *Nat. Rev. Cancer* **2008**, *8*, 180.

[21] G. Yang, L. Xu, Y. Chao, J. Xu, X. Sun, Y. Wu, R. Peng, Z. Liu, *Nat. Commun.* **2017**, *8*, 902.

[22] C. He, D. Liu, W. Lin, *ACS Nano* **2015**, *9*, 991.

[23] S. Goel, C. A. Ferreira, F. Chen, P. A. Ellison, C. M. Siamof, T. E. Barnhart, W. Cai, *Adv. Mater.* **2018**, *30*, 1704367.

[24] Y. Cheng, H. Cheng, C. Jiang, X. Qiu, K. Wang, W. Huan, A. Yuan, J. Wu, Y. Hu, *Nat. Commun.* **2015**, *6*, 8785.

[25] Y. Kuang, K. Balakrishnan, V. Gandhi, X. Peng, *J. Am. Chem. Soc.* **2011**, *133*, 19278.

[26] T. P. Szatrowski, C. F. Nathan, *Cancer Res.* **1991**, *51*, 794.

[27] M. Huo, L. Wang, Y. Chen, J. Shi, *Nat. Commun.* **2017**, *8*, 357.

[28] J. D. Lambeth, *Nat. Rev. Immunol.* **2004**, *4*, 181.

[29] W. Fan, W. Bu, B. Shen, Q. He, Z. Cui, Y. Liu, X. Zheng, K. Zhao, J. Shi, *Adv. Mater.* **2015**, *27*, 4155.

[30] J. Xu, W. Han, P. Yang, T. Jia, S. Dong, H. Bi, A. Gulzar, D. Yang, S. Gai, F. He, J. Lin, C. Li, *Adv. Funct. Mater.* **2018**, *28*, 1803804.

[31] Z. Ma, X. Jia, J. Bai, Y. Ruan, C. Wang, J. Li, M. Zhang, X. Jiang, *Adv. Funct. Mater.* **2017**, *27*, 1604258.

[32] C. C. Huang, W. T. Chia, M. F. Chung, K. J. Lin, C. W. Hsiao, C. Jin, W. H. Lim, C. C. Chen, H. W. Sung, *J. Am. Chem. Soc.* **2016**, *138*, 5222.

[33] L.-H. Liu, Y.-H. Zhang, W.-X. Qiu, L. Zhang, F. Gao, B. Li, L. Xu, J.-X. Fan, Z.-H. Li, X.-Z. Zhang, *Small* **2017**, *13*, 1701621.

[34] D. W. Zheng, B. Li, C. X. Li, J. X. Fan, Q. Lei, C. Li, Z. Xu, X. Z. Zhang, *ACS Nano* **2016**, *10*, 8715.

[35] Z. Ma, M. Zhang, X. Jia, J. Bai, Y. Ruan, C. Wang, X. Sun, X. Jiang, *Small* **2016**, *12*, 5477.

[36] Q. Annu Rev Biomed EngJia, J. Ge, W. Liu, X. Zheng, S. Chen, Y. Wen, H. Zhang, P. Wang, *Adv. Mater.* **2018**, *30*, 6069.

[37] J. Ge, Q. Jia, W. Liu, M. Lan, B. Zhou, L. Guo, H. Zhou, H. Zhang, Y. Wang, Y. Gu, X. Meng, P. Wang, *Adv. Healthcare Mater.* **2016**, *5*, 665.

[38] D. Yang, G. Yang, Q. Sun, S. Gai, F. He, Y. Dai, C. Zhong, P. Yang, *Adv. Healthcare Mater.* **2018**, *7*, 1800042.

[39] H. Cheng, J.-Y. Zhu, S.-Y. Li, J.-Y. Zeng, Q. Lei, K. W. Chen, C. Zhang, X.-Z. Zhang, *Adv. Funct. Mater.* **2016**, *26*, 7847.

[40] Y. Yang, W. Zhu, L. Feng, Y. Chao, X. Yi, Z. Dong, K. Yang, W. Tan, Z. Liu, M. Chen, *Nano Lett.* **2018**, *18*, 6867.

[41] H. Wang, Y. Chao, J. Liu, W. Zhu, G. Wang, L. Xu, Z. Liu, *Biomaterials* **2018**, *181*, 310.

[42] Y. Liu, W. Zhen, L. Jin, S. Zhang, G. Sun, T. Zhang, X. Xu, S. Song, Y. Wang, J. Liu, H. Zhang, *ACS Nano* **2018**, *12*, 4886.

[43] J. Kim, H. R. Cho, H. Jeon, D. Kim, C. Song, N. Lee, S. H. Choi, T. Hyeon, *J. Am. Chem. Soc.* **2017**, *139*, 10992.

[44] Y. Zhang, F. Wang, C. Liu, Z. Wang, L. Kang, Y. Huang, K. Dong, J. Ren, X. Qu, *ACS Nano* **2018**, *12*, 651.

[45] D. Wang, R. Shi, J. Zhou, S. Shi, H. Wu, P. Xu, H. Wang, G. Xia, T. E. Barnhart, W. Cai, Z. Guo, Q. Chen, *iScience* **2018**, *9*, 14.

[46] J. Ge, M. Lan, B. Zhou, W. Liu, L. Guo, H. Wang, Q. Jia, G. Niu, X. Huang, H. Zhou, X. Meng, P. Wang, C.-S. Lee, W. Zhang, X. Han, *Nat. Commun.* **2014**, *5*, 4596.

[47] W. Zhen, Y. Liu, L. Lin, J. Bai, X. Jia, H. Tian, X. Jiang, *Angew. Chem. Int. Ed.* **2018**, *57*, 10309.

[48] G. Calixto, J. Bernegossi, L. de Freitas, C. Fontana, M. Chorilli, *Molecules* **2016**, *21*, 342.

[49] M. Triesscheijn, P. Baas, J. H. M. Schellens, F. A. Stewart, *Oncologist* **2006**, *11*, 1034.

[50] L. Romero-Castillo, I. Posadas, V. Ceña, *Can. J. Chem.* **2017**, *95*, 917.

[51] R. D. Brohi, L. Wang, H. S. Talpur, D. Wu, F. A. Khan, D. Bhattarai, Z. U. Rehman, F. Farmanullah, L. J. Huo, *Front. Pharmacol.* **2017**, *8*, 606.

[52] V. Srivastava, D. Gusain, Y. C. Sharma, *Ind. Eng. Chem. Res.* **2015**, *54*, 6209.

[53] D. Wang, H. Wu, J. Zhou, P. Xu, C. Wang, R. Shi, H. Wang, H. Wang, Z. Guo, Q. Chen, *Adv. Sci.* **2018**, *5*, 1800287.

[54] D. Wang, Z. Guo, J. Zhou, J. Chen, G. Zhao, R. Chen, M. He, Z. Liu, H. Wang, Q. Chen, *Small* **2015**, *11*, 5956.

[55] Z. Li, C. Wang, L. Cheng, H. Gong, S. Yin, Q. Gong, Y. Li, Z. Liu, *Biomaterials* **2013**, *34*, 9160.

[56] Q. Chen, L. Feng, J. Liu, W. Zhu, Z. Dong, Y. Wu, Z. Liu, *Adv. Mater.* **2016**, *28*, 7129.

[57] H. Wang, X. Yang, W. Shao, S. Chen, J. Xie, X. Zhang, J. Wang, Y. Xie, *J. Am. Chem. Soc.* **2015**, *137*, 11376.

[58] J. Chen, H. Luo, Y. Liu, W. Zhang, H. Li, T. Luo, K. Zhang, Y. Zhao, J. Liu, *ACS Nano* **2017**, *11*, 12849.

[59] Q. F. Li, X. R. Wang, Y. W. Yang, H. Lin, *Cell Res.* **2006**, *16*, 548.

[60] M. McNutt, *Science* **2013**, *342*, 1417.

[61] F. Yuan, M. Dellian, D. Fukumura, M. Leunig, D. A. Berk, V. P. Torchilin, R. K. Jain, *Cancer Res.* **1995**, *55*, 3752.

[62] S. K. Hobbs, W. L. Monsky, F. Yuan, W. G. Roberts, L. Griffith, V. P. Torchilin, R. K. Jain, *Proc. Natl. Acad. Sci. U.S.A.* **1998**, *95*, 4607.

[63] H. Maeda, J. Wu, T. Sawa, Y. Matsumura, K. Hori, *J. Controlled Release* **2000**, *65*, 271.

[64] J. B. Liu, M. X. Yu, C. Zhou, S. Y. Yang, X. H. Ning, J. Zheng, *J. Am. Chem. Soc.* **2013**, *135*, 4978.

[65] L. Brannon-Peppas, J. O. Blanchette, *Adv. Drug Delivery Rev.* **2012**, *64*, 206.

[66] L. Zhang, F. Gu, J. Chan, A. Wang, R. Langer, O. Farokhzad, *Clin. Pharmacol. Ther.* **2008**, *83*, 761.

[67] X. Song, L. Feng, C. Liang, K. Yang, Z. Liu, *Nano Lett.* **2016**, *16*, 6145.

[68] J. J. Liu, Y. Yang, W. W. Zhu, X. Yi, Z. L. Dong, X. N. Xu, M. W. Chen, K. Yang, G. Lu, L. X. Jiang, Z. Liu, *Biomaterials* **2016**, *97*, 1.

[69] P. Xu, H. Wu, D. Wang, G. Zhao, F. Li, B. Qiu, Z. Guo, Q. Chen, *Adv. Healthcare Mater.* **2018**, *7*, 1800322.

[70] P. Zhu, Y. Chen, J. Shi, *ACS Nano* **2018**, *12*, 3780.

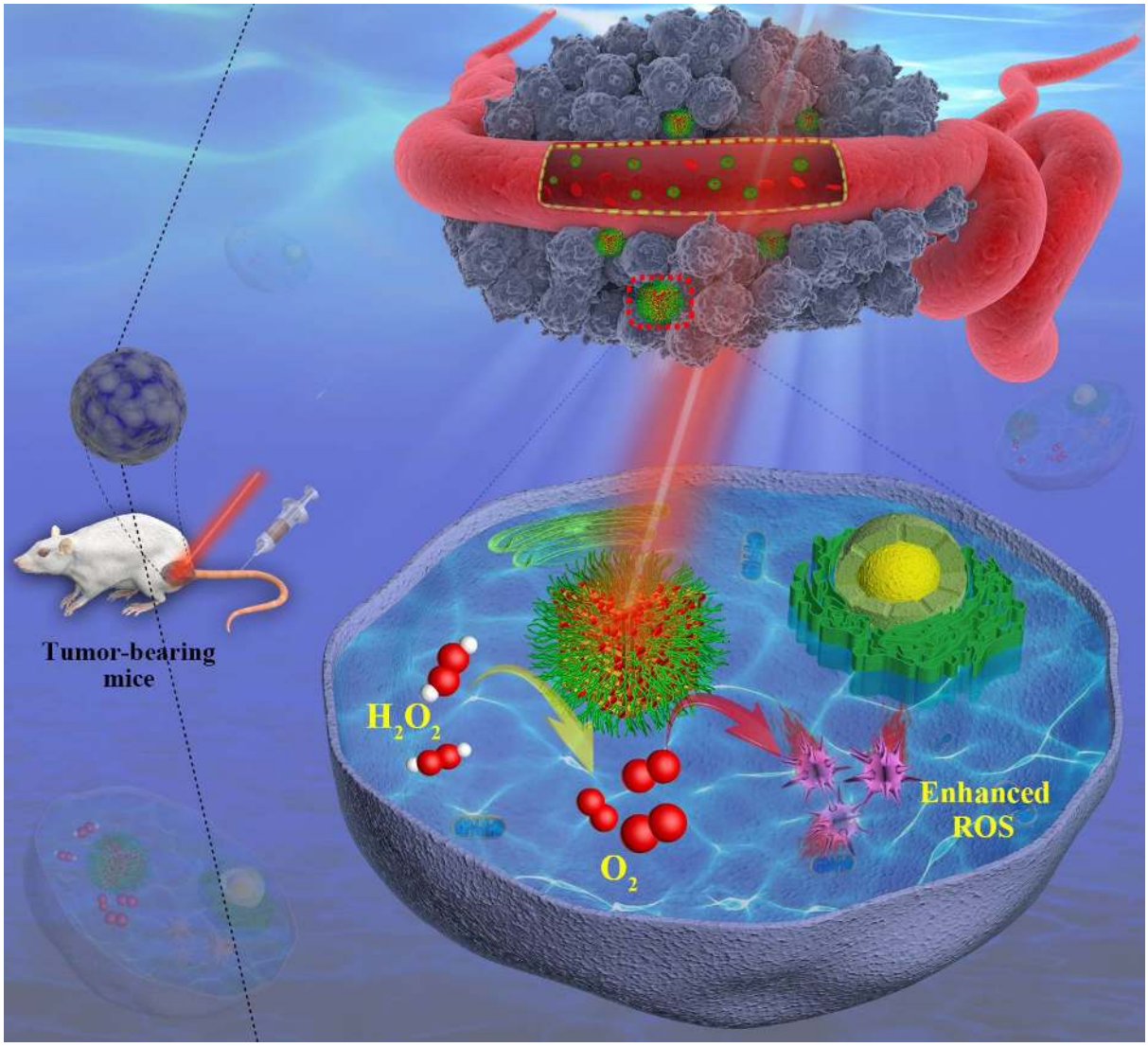

Scheme 1. Schematic illustration of MOF-derived mesoporous NE for enhanced PDT of cancer.

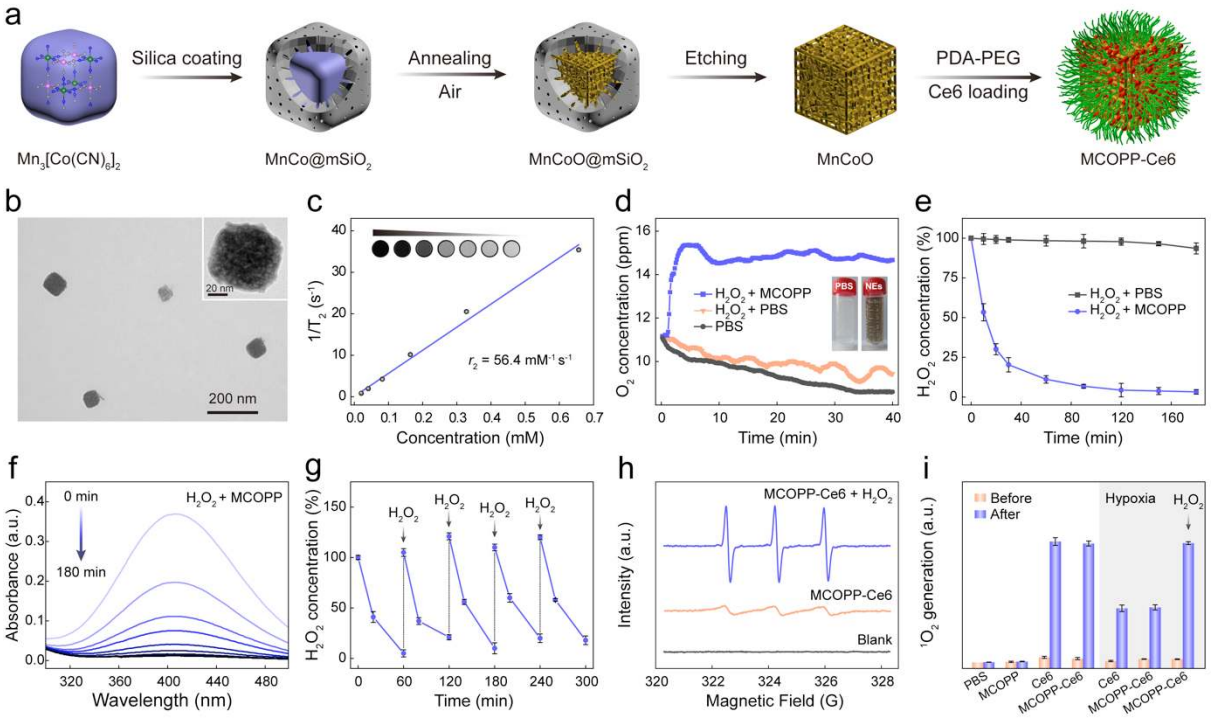

Figure 1. Synthesis of MCOPP NE along with structure and property characterizations. (a) Schematic representation for the preparation of MCOPP NE. (b) TEM image of MCOPP NE. (c) Plot of $1/T_2$ as a function of Mn concentration. The inset shows MRI phantom images of MCOPP NE. (d) O_2 generation after treating with MCOPP NE in PBS. The inset shows photographs of H_2O_2 solutions with and without MCOPP NE. (e) Degradation of H_2O_2 with and without MCOPP NE. (f) Corresponding absorption spectra of H_2O_2-$Ti(SO_4)_2$ solution in the presence of MCOPP NE. (g) Repetitive catalytic ability of MCOPP NE with repetitive addition of H_2O_2. (h) ESR spectra of $^1O_2$ trapped by TEMP under different conditions after 671 nm laser (100 mW cm^{-2}) irradiation for 10 seconds. (i) The $^1O_2$ generation efficiency determined by DPBF under various conditions before and after 671 nm laser (100 mW cm^{-2}, 30 min) irradiation.

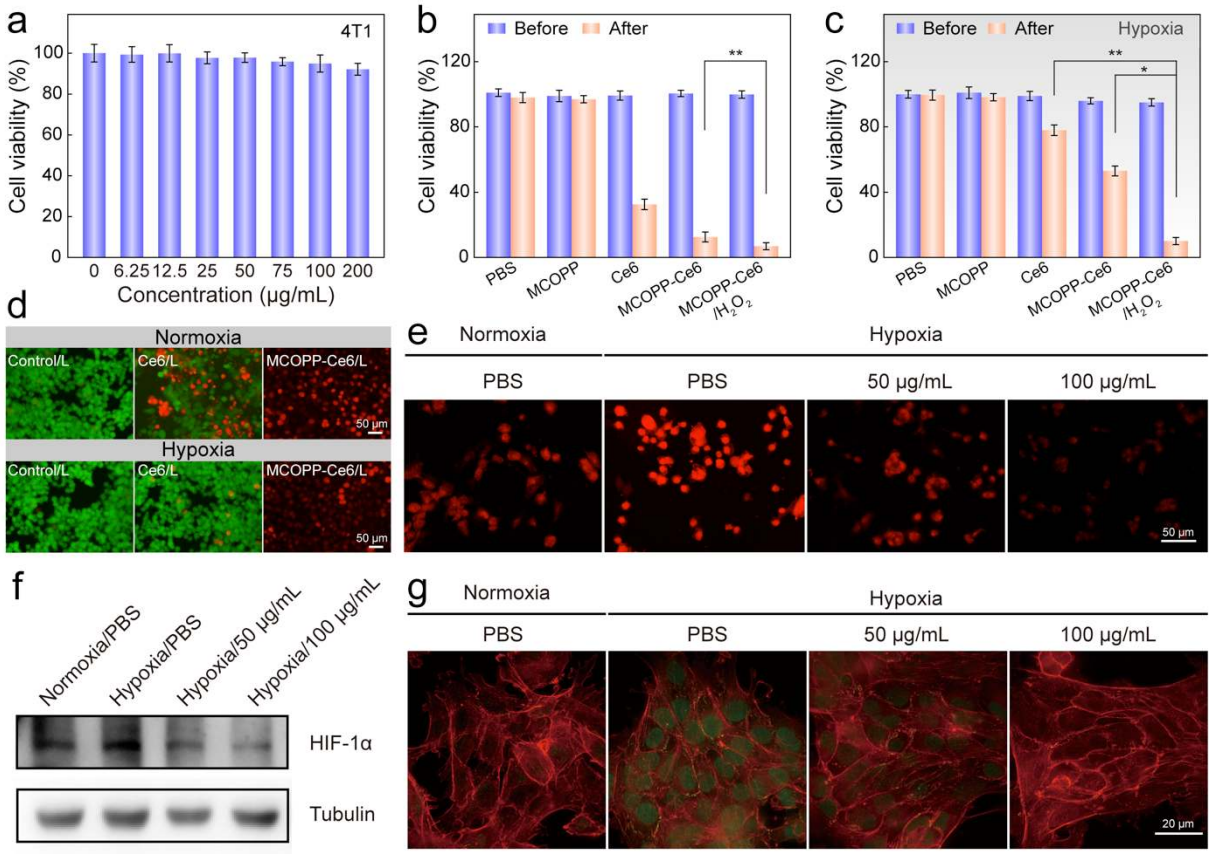

Figure 2. *In vitro* therapy of MCOPP NE. (a) Viability of 4T1 cells treated with MCOPP NE at different concentrations. Cell viability assay of 4T1 cells treated under different conditions in (b) normoxic and (c) hypoxic environments before and after 671 nm laser light irradiation. (d) Live/dead cell assay for cells treated with PBS, free Ce6 and MCOPP-Ce6 under normoxic and hypoxic conditions (green: live cells, red: dead cells). (e) CLSM images of 4T1 cells stained by O_2 indicator, *i.e.*, $(Ru(dpp)_3)Cl_2$, after different treatments. (f) Western blots of HIF-1α expression in 4T1 cells treated with MCOPP NE. (g) CLSM images of HIF-1α (green) and F-actin (red) in cells incubated with MCOPP NE under normoxic and hypoxic conditions. Statistical analysis was performed using the Student's two-tailed t-test (*$p < 0.05$ and **$p < 0.01$).

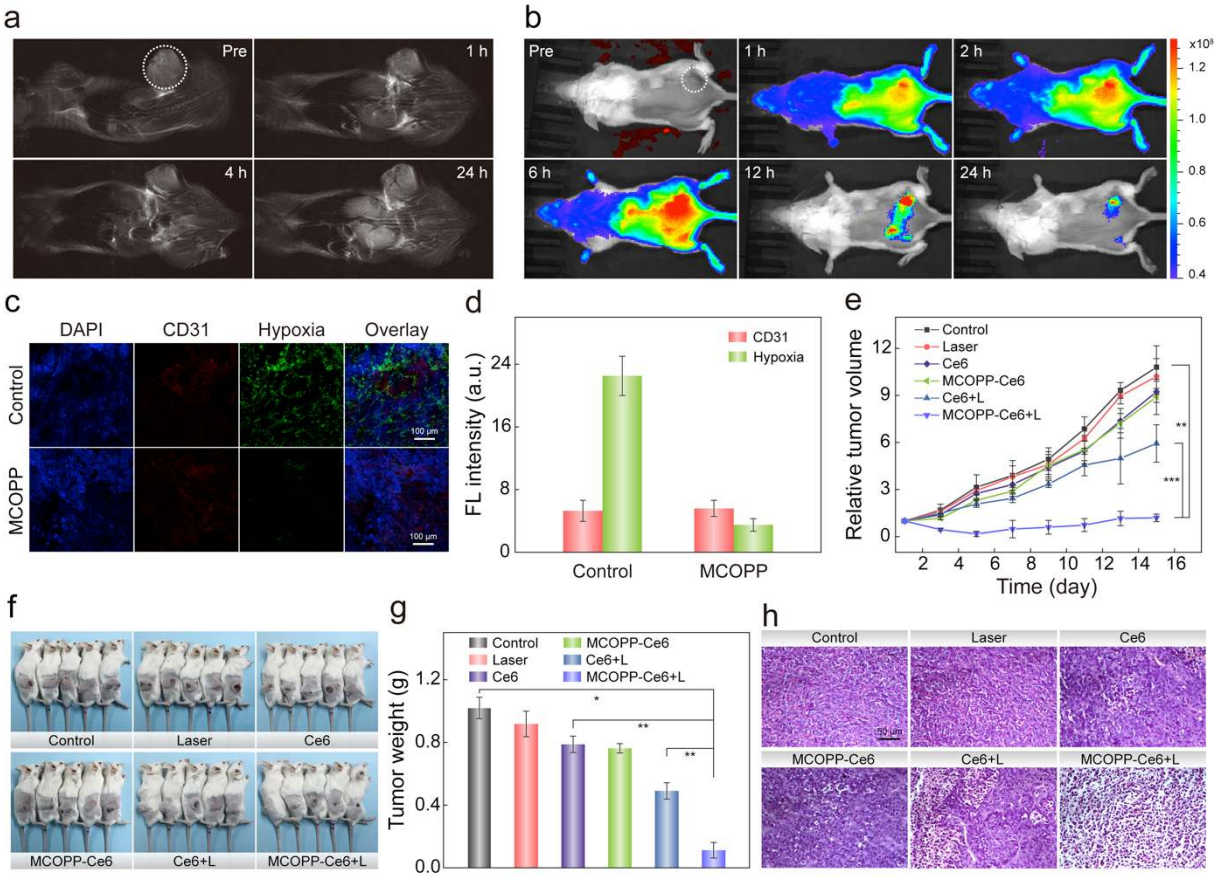

Figure 3. *In vivo* imaging and therapy. (a) *In vivo* T_2*-weighted MR images of 4T1-tumor-bearing mouse at various time periods. (b) *In vivo* fluorescence images of 4T1-tumor-bearing mouse *via* intravenous injection with MCOPP-Ce6 (equivalent Ce6 amount is 4 mg/kg body) at different times. Tumors are circled with white dashed lines. (c) Representative immunofluorescence images of tumor slices after hypoxia staining. The hypoxia areas and blood vessels were stained by anti-pimonidazole antibody (green) and anti-CD31 antibody (red). (d) Relative hypoxia positive areas and blood vessel density measured using the ImageJ software. (e) Relative tumor volume of mice after various treatments (n = 5), *i.e.*, I (control), II (laser), III (Ce6), IV (MCOPP-Ce6), V (Ce6 + laser), and VI (MCOPP-Ce6 + laser). (f) Photographic images of mice at the end of these treatments. (g) Average weights of tumors harvested at the end of these treatments. (h) Histological analysis of tumor tissues stained with hematoxylin and eosin from these groups. Statistical analysis was performed using the Student's two-tailed t-test (*p <0.05, **p <0.01 and ***p <0.001).

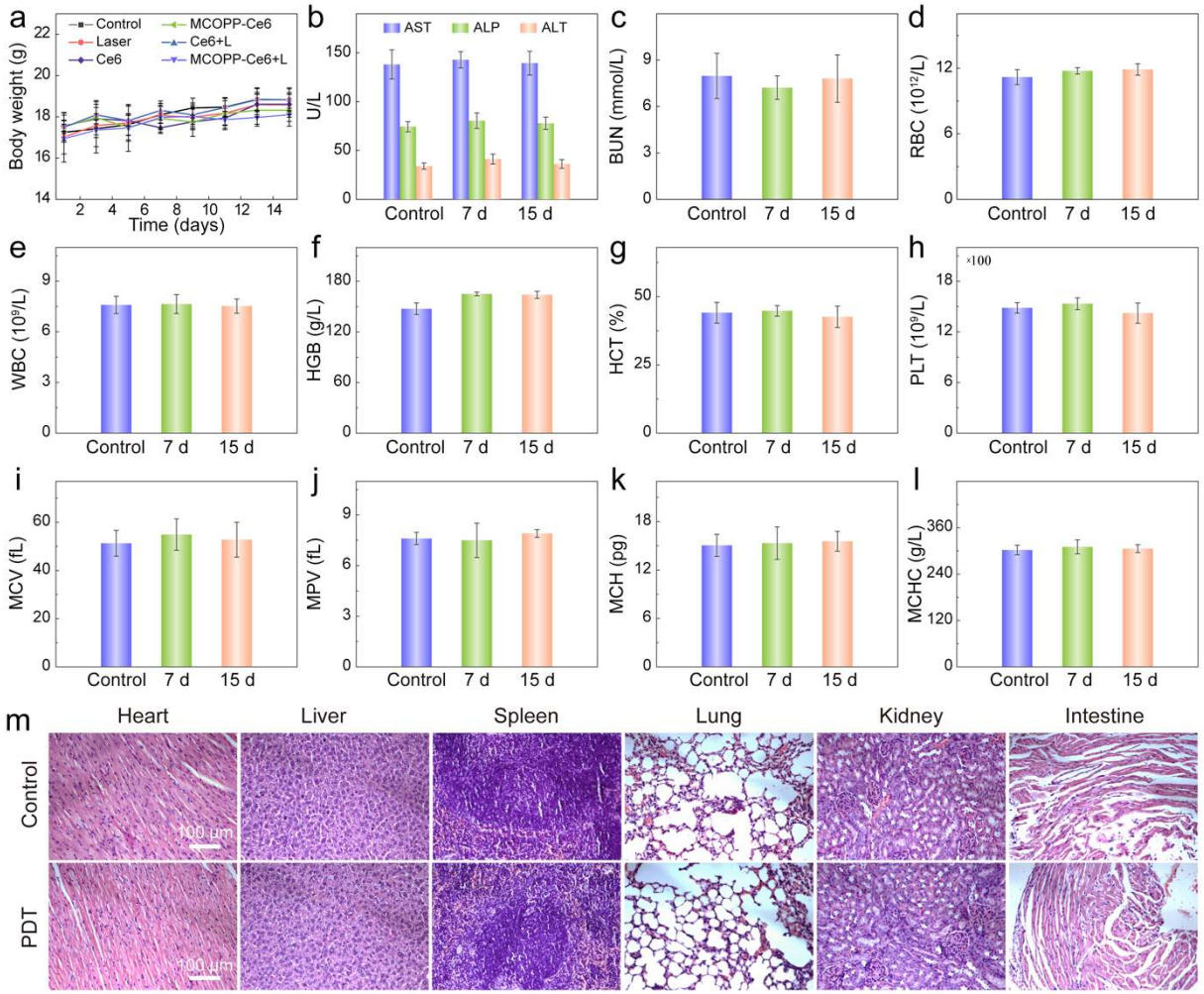

Figure 4. *In vivo* toxicity assessments. (a) Average body weights of mice after different treatments indicated during the whole therapy process. (b) Levels of AST, ALP, and ALT, as well as (c) BUN of untreated mice (control) and MCOPP-Ce6 injected mice at 7 d and 15 d. (d-l) Hematology data of untreated mice (control) and mice treated with MCOPP-Ce6 at 7 d and 15 d. (m) Histological analysis of the main organs (heart, liver, spleen, lung, kidney, and intestine) of untreated mice (control) and mice treated with MCOPP-Ce6 + laser.

Table of Contents Graphic

A biocompatible mesoporous nanoenzyme derived from metal-organic frameworks is developed to alleviate the tumor hypoxia. The nanoenzyme could highly catalyze H_2O_2 for endogenous O_2 generation both *in vitro* and *in vivo* without any external activation, demonstrating enhanced photodynamic therapy efficacy in the cancer treatment.

Mesoporous Nanoenzyme Derived from Metal-Organic Frameworks with Endogenous Oxygen Generation to Alleviate Tumor Hypoxia for Significantly Enhanced Photodynamic Therapy

Dongdong Wang, Huihui Wu, Wei Qi Lim, Soo Zeng Fiona Phua, Pengping Xu, Qianwang Chen,* Zhen Guo,* Yanli Zhao*

Keywords: endogenous oxygenation • H_2O_2-activation • hypoxia alleviation • metal-organic frameworks • photodynamic therapy